Geophysical Research Letters

RESEARCH LETTER
10.1029/2025GL120143

Splay Fault Permeability Governs Fluid–Structure Interaction in Accretionary Wedges

Joaquin Julve[1], Åke Fagereng[1], Giovanni Toffol[1], and Kohtaro Ujiie[2]

[1]School of Earth and Environmental Sciences, Cardiff University, Cardiff, UK, [2]Graduate School of Science and Technology, University of Tsukuba, Tsukuba, Japan

Key Points:

- Poroelastic finite element models are applied to predict the effect of splay fault permeability on long-term stress and deformation patterns
- Impermeable splay faults trap footwall fluids and encourage footwall dilatancy; permeable splay faults channel fluids and enhance time-integrated fluid flow in the wedge
- Permeable splay faults maintain megathrust overpressures and enhance creep, whereas megathrust seismicity is promoted by impermeable splays

Supporting Information:

Supporting Information may be found in the online version of this article.

Correspondence to:

J. Julve,
julvelilloj@cardiff.ac.uk

Citation:

Julve, J., Fagereng, Å., Toffol, G., & Ujiie, K. (2026). Splay fault permeability governs fluid–structure interaction in accretionary wedges. *Geophysical Research Letters*, *53*, e2025GL120143. https://doi.org/10.1029/2025GL120143

Received 21 OCT 2025
Accepted 18 FEB 2026

Author Contributions:

Conceptualization: Joaquin Julve, Åke Fagereng, Giovanni Toffol, Kohtaro Ujiie
Data curation: Joaquin Julve
Investigation: Joaquin Julve, Giovanni Toffol
Methodology: Joaquin Julve
Supervision: Åke Fagereng
Validation: Åke Fagereng
Visualization: Joaquin Julve, Åke Fagereng, Kohtaro Ujiie
Writing – original draft: Joaquin Julve
Writing – review & editing: Åke Fagereng, Giovanni Toffol, Kohtaro Ujiie

Abstract Interactions between upper plate deformation and plate interface seismicity in subduction zones remain poorly understood, but growing evidence indicates that fluid flow along splay faults modulates upper-plate faulting. Field observations from two exhumed splay faults define end-member scenarios where impermeable faults trap fluids in their footwall, whereas permeable faults channel fluids along them. Using finite element poroelastic models, with slip mode inferred solely from stress–pore-fluid pressure patterns, we define two end-member behaviors: (a) Impermeable, clay-rich, mature splay faults favor footwall fluid flow, promoting low differential stress, dilation, and vein formation in the upper plate, while reducing pore-fluid pressure and coupling the megathrust downdip of the intersection. (b) Permeable, less mature faults allow distributed upper-plate fluid flow, increasing fluid flux, and differential stress, while maintaining plate interface overpressure and promoting creep. These models provide a framework for prism-scale effects of splay fault permeability on shallow subduction zone deformation and seismicity.

Plain Language Summary Subduction zones are areas where one tectonic plate slides beneath another, and they produce the world's largest earthquakes. In these settings, faults called *splay faults* cut through the upper plate and connect to the deeper plate boundary fault. Fluids circulating in these zones—like water trapped in the rocks—can influence whether faults slowly slip or break suddenly in earthquakes. But how these fluids move, and what controls their pathways, is still not fully understood. This study combines geological observations of ancient, exposed splay faults in Japan with computer simulations that track how fluids and rock deformation interact over thousands of years. The results show that the *permeability* of splay faults—that is, how easily fluids can move along or through them—is a key factor that shapes where fluids go, how rocks break, and where earthquake-related features like veins can form. These findings help connect short-term geophysical observations with long-term geological processes. Understanding the role of fault permeability may improve how we assess earthquake hazards in areas where fluids and complex fault systems interact.

1. Introduction

Subduction plate interfaces host the largest earthquakes. Their size and impact reflect coupling between fluid circulation and deformation along the megathrust and within the upper plate (e.g., Bassett et al., 2025; Bilek & Lay, 2018). Observations show that slip along the megathrust and across the accretionary prism spans a continuum from slow slip to seismic rupture (Kirkpatrick et al., 2021; Leeman et al., 2016; Peng & Gomberg, 2010). This behavior is driven by variations in fault friction (e.g., Barbot, 2019), which are closely linked to the fault's hydraulic state (e.g., Garagash, 2021). Splay faults rooted at the plate interface partition deformation between the megathrust and upper plate (e.g., Haeussler et al., 2015; Park et al., 2002) and redistribute fluids within the overriding plate (e.g., Cortés-Rivas et al., 2025; Watson et al., 2019). These processes together influence megathrust and upper plate behavior, yet the role of splay fault permeability in modulating deformation remains poorly constrained. Here we use numerical models to explore the effect of changes in splay fault permeability on fluid flow and deformation across outer accretionary prisms.

Previous modeling efforts have addressed various aspects of fluid–rock interaction in subduction zones: fluid budgets in accretionary prisms from porosity loss and dehydration reactions (Ellis et al., 2015); coupling of compaction, permeability, and pore-fluid pressure to assess megathrust strength (Sun et al., 2020); permeable splay faults focusing fluid flow from dehydration reactions (Lauer & Saffer, 2015); and the accumulation of stress under viscoelastic conditions (Muramoto et al., 2023). However, models are yet to explicitly explore how splay

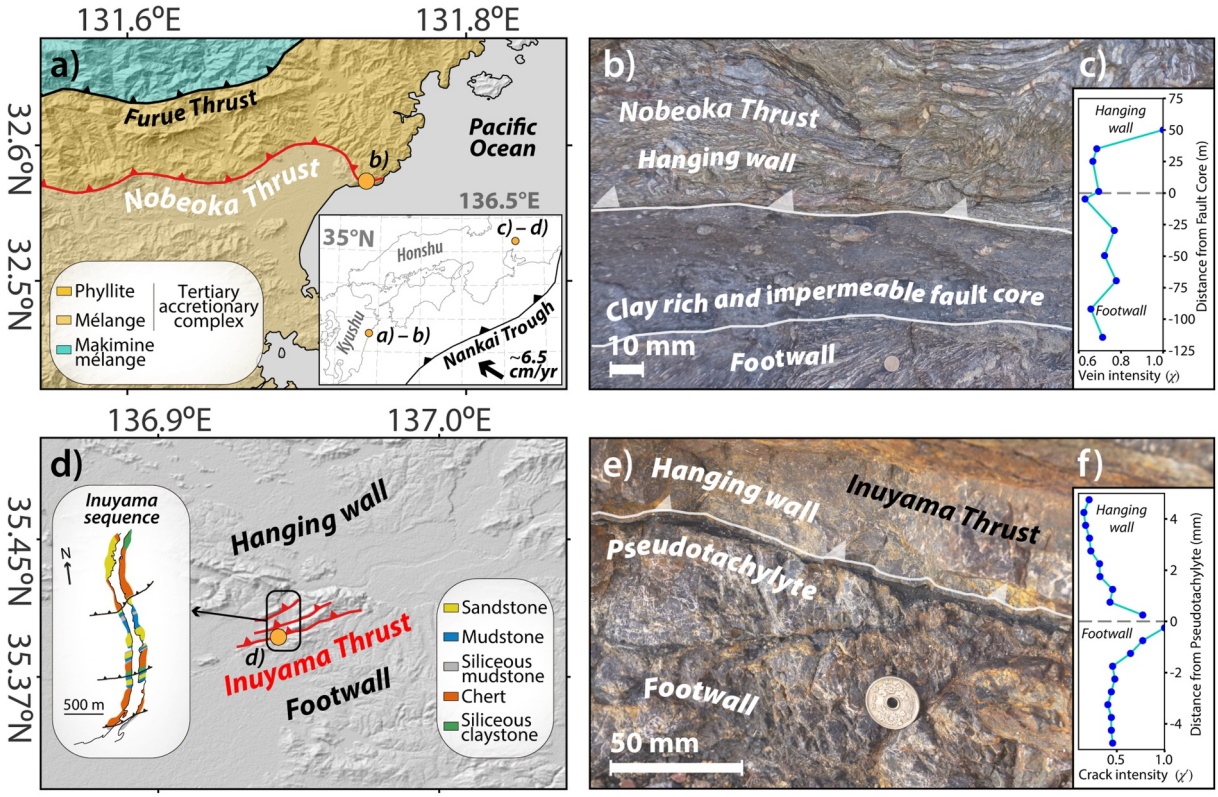

Figure 1. Natural examples of exhumed splay fault systems onshore from the Nankai Trough: (a–c) the Nobeoka Thrust and (d–f) the Inuyama thrust. Panel (c) is the vein intensity distribution (χ) in Nobeoka Thrust from Otsubo et al. (2020). The sequence in panel (d) is from Ujiie et al. (2021). (f) Is the crack intensity (χ') against distance to the pseudotachylyte (Ujiie et al., 2021). Red and white solid lines mark the main thrusts observed at outcrop scale. Footwall and Hanging wall are defined with respect to the splay fault, not the megathrust. Topography is from NASA Shuttle Radar Topography Mission (2013).

fault permeability governs long-term pore-fluid pressure evolution, stress state, deformation, and the distribution of seismicity within accretionary wedges.

Inspired by geological observations from exhumed splay fault systems in Japan (Figure 1), we hypothesize that permeability within splay faults controls long-term fluid flow, directly influencing the distribution of deformation and megathrust seismicity. In particular, the Nobeoka Thrust (Figures 1a–1c) is a regionally extensive splay fault juxtaposing the northern and southern Shimanto Belt, characterized by a clay-rich, low-permeability core, extensive footwall vein systems (Kondo et al., 2005) and local hanging wall pseudotachylytes indicative of seismic slip events (Hasegawa et al., 2019). In contrast, the Inuyama thrust (Figures 1d–1f), which is a tens-of-kilometers-scale fault developed within a chert-rich wall rock, records seismicity but limited evidence for fluid-assisted deformation structures (Ujiie et al., 2021). These examples illustrate how variations in lithology and structural permeability influence fracture patterns and fluid retention across splay fault systems. Notably, given that tensile veins form under specific stress and pore-fluid pressure conditions (Secor, 1965), the abundance of mineralized veins in the footwall of the Nobeoka Thrust, compared to their scarcity at Inuyama (Figures 1b, 1c, 1e, and 1f), provides a geological record that can be used to evaluate numerical simulation outcomes.

To test this hypothesis, we construct poroelastic numerical models quantifying how splay fault permeability governs stress, pore-fluid pressure, and deformation evolution in the outer wedge. We present the numerical implementation and an updated permeability–porosity formulation, then explore fluid flow and vein formation under contrasting permeability conditions. Comparing model results with geophysical data from the Nankai Trough (Japan) and northern Hikurangi (New Zealand), we reconcile geological and geophysical evidence for splay fault roles in modulating fluid distribution, stress and deformation patterns, and seismic behavior in subduction zones. Throughout, hanging wall and footwall refer to domains above and below the splay fault, respectively—not the megathrust.

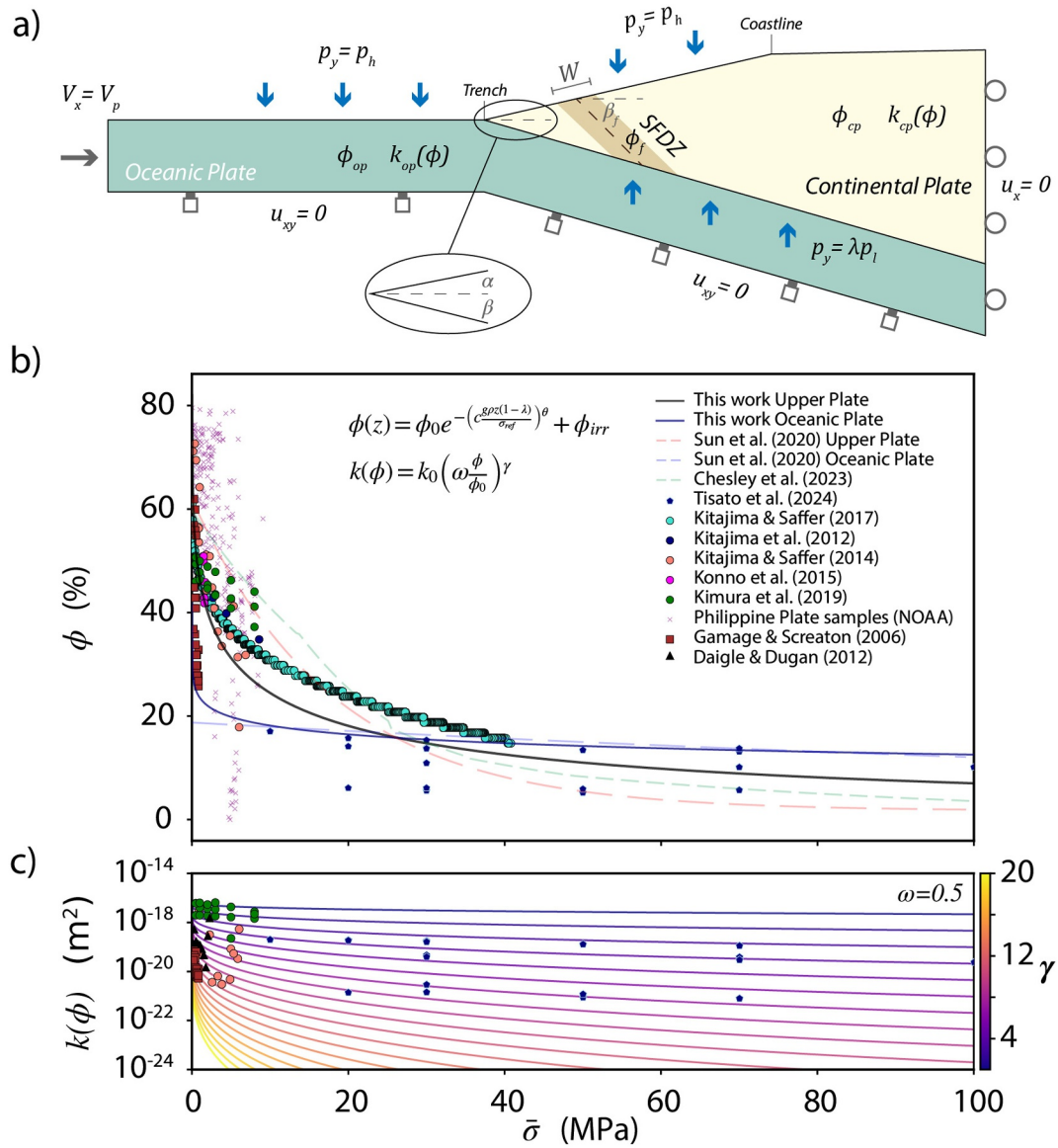

Figure 2. Model setup and distributions of porosity and permeability with $\bar{\sigma}$. Subscripts cp, f, and op refer to the continental plate, fault zone, and oceanic plate, respectively. (a) Numerical model framework. P_y is fluid pressure along the vertical axis, defined as either hydrostatic (P_h) or a fraction (λ) of lithostatic ($P_l = g\rho z$). A constant velocity $V_x = V_p = 10^{-9}$ (m/s) is imposed at the rear of the oceanic plate. Displacement boundary conditions $u_{xy} = 0$ and $u_x = 0$ are applied at the base of the oceanic and continental plates, respectively. Circles denote traction-free vertical boundaries; squares indicate fixed displacements. (b) Compilation of porosity data as a function of effective vertical stress. Curves follow Equation 1, and data set details are provided in Table S1 in Supporting Information S1. (c) Permeability as a function of effective stress. Colored lines represent Equation 2 with $\omega = 0.5$ and varying γ values; symbols correspond to laboratory and field data sets labeled in panel (b).

2. Data and Methods

2.1. Numerical Model

To evaluate the influence of splay fault permeability on offshore wedge deformation and seismicity, we model long-term volumetric strain rate $\left(\dot{\epsilon}_v\right)$ and Cauchy stress tensor $(\boldsymbol{\sigma})$ as functions of fluid content (ζ) and pore-fluid pressure $\left(P_f\right)$ in a poroelastic accretionary prism containing a splay fault of variable permeability (Figure 2a). Using PyLith (Aagaard et al., 2013; Walker et al., 2023), we solve conservation of linear momentum and enforce

fluid mass balance (Text S1 in Supporting Information S1), modeling a slightly compressible fluid ($0 < 1/K_f \ll 1$, where K_f is the fluid bulk modulus, Text S1 in Supporting Information S1) saturating a porous solid under infinitesimal strain. The system assumes $\dot{\epsilon}_v$ depends on permeability (k) and porosity (ϕ) of oceanic and continental rocks, where the plate interface can deform freely.

Following simplified wedge geometry (Noda, 2016), the oceanic plate subducts at constant dip $\beta = 12°$, while the accretionary prism seafloor has slope $\alpha = 2°$ offshore of the coastline, 150 km from the trench. Within the accretionary prism, the splay fault damage zone (SFDZ) is represented as a constant-width zone of $W = 2$ (km) dipping landward at $\beta_f = 20°$. Although natural damage zones are typically tens to hundreds of meters wide (Savage & Brodsky, 2011), reducing W from 2 to 0.5 (km) produces no statistically significant changes in $\dot{\epsilon}_v$, $\boldsymbol{\sigma}$, or P_f (within 95% confidence; Figures S1 and S2 in Supporting Information S1). We therefore adopt $W = 2$ (km) to reduce computational cost. Initial P_f conditions are hydrostatic at the sea floor (Figure 2a). Along the plate interface, initial P_f is set as $P_f = \lambda P_l$, where $\lambda = 0.85$ is the pore-fluid pressure ratio and $P_l = g\rho z$ is lithostatic pressure, with g as the gravitational acceleration, ρ as the average upper plate density, and z as depth. For simplicity, no subduction channel is assumed.

Both the oceanic and continental plates are poroelastic. We impose a convergence velocity at the seaward rear of the oceanic plate ($V_x = V_p = 10^{-9}$ (m/s)). Displacements are fixed at the base of the oceanic plate ($u_{xy} = 0$) and landward rear of the continental plate ($u_x = 0$); the seafloor and surface remain traction-free. PyLith solves for ζ and P_f via Darcy's flux ($\vec{q}$), which depends on permeability k, and accounts for specific storage linked to porosity ϕ (Text S1 in Supporting Information S1). Stress and strain evolve in response to k-driven variations in P_f, with material properties constrained by global subduction zone data sets (Figure 2 and Table S3 in Supporting Information S1).

We perform quasi-static simulations over 2,000 years to characterize outer wedge deformation. Principal stresses are extracted via eigenvalue decomposition of $\boldsymbol{\sigma}$; eigenvalues define magnitudes and eigenvectors the orientations. Meshing, governing equations, and parameter details are provided in Text S1, Table S1, and Figure S3 in Supporting Information S1.

2.2. Porosity

We analyze porosity depth-dependence using an updated exponential formulation capturing fine-grained marine sediment consolidation behavior (Sun et al., 2020), calibrated against compiled porosity versus effective stress data sets (Figure 2b and Table S2 in Supporting Information S1). Effective stress is defined as $\bar{\sigma} = P_l - P_f$. The porosity ϕ is modeled as:

$$\phi = \phi_0 e^{-\left(c\frac{g\rho z(1-\lambda)}{\bar{\sigma}_{\text{ref}}}\right)^{\theta}} + \phi_{\text{irr}} \tag{1}$$

Here, ϕ_0 is the reference porosity, ϕ_{irr} is irreducible porosity, and $\bar{\sigma}_{\text{ref}}$ is a reference effective stress. The parameter c is a compaction efficiency describing how readily porosity is lost with loading, analogous to coefficients in Terzaghi's consolidation theory (Parasnis, 1960; Terzaghi, 1943). The exponent θ captures non-linear grain-scale compaction mechanisms such as particle rearrangement, pressure solution, cementation, and microfracture collapse (F. M. Chester et al., 2007; J. Chester et al., 2004; Fisher et al., 1999). This formulation parallels the stretched exponential models of viscoelastic and porous systems (G. Williams & Watts, 1970), with $0 < \theta \leq 1$.

Figure 2b presents our preferred porosity profiles. For the continental plate, we use $c = 2.5$ and $\theta = 1/3$; for the oceanic plate, $c = 1$ and $\theta = 1/6$. Prior studies used $c = 1$ and $\theta = 1$ (Sun et al., 2020), but we prefer our values as they better emulate the sharp decrease in porosity, to a near constant value, that occurs at $\bar{\sigma} < \sim$10 MPa (Figure 2b). To simulate the effect of the splay fault (Figure 2a) we apply an exponential perturbation in ϕ toward the fault axis, increasing or decreasing it depending on whether the fault is modeled as permeable or impermeable. This perturbation is a function of the distance ratio d/W, where d is the shortest distance from a mesh element to the fault axis (Text S2 in Supporting Information S1).

2.3. Permeability

Permeability k is prescribed as a function of porosity ϕ following a Kozeny–Carman type relation (Hommel et al., 2018, and references therein):

$$k = k_0\left(\omega\frac{\phi}{\phi_0}\right)^{\gamma} \tag{2}$$

Here, k_0 is the reference permeability. The parameter ω represents the efficiency with which connected porosity contributes to hydraulic conductivity, encapsulating combined effects of pore connectivity and network tortuosity (Amaefule et al., 1993). Larger ω values correspond to more efficiently connected pore networks and therefore higher permeability for a given porosity (Figures S6 and S7 in Supporting Information S1). The exponent γ quantifies permeability sensitivity to porosity, reflecting how pore geometry and connectivity evolve during compaction, cementation, or structural collapse (Civan, 2001). Higher γ values yield a sharper reduction in k with decreasing ϕ, capturing non-linear permeability degradation.

Because $k(\phi)$ inherits the spatial gradients of ϕ, the exponential porosity profile across the fault zone (W) directly generates permeability contrasts (Text S2 in Supporting Information S1), enabling both permeable and impermeable fault scenarios. Figure 2b illustrates the sensitivity of k to γ. In our models, we vary γ while keeping $\omega = 0.5$, as it better represents available data (Figures S6 and S7 in Supporting Information S1). This sets the initial magnitude of k and is constrained by available data sets (Figure 2c). All the parameters used are listed in Table S3 in Supporting Information S1.

2.4. Tensile Fracture and Vein Formation Criterion

Exhumed splay fault systems (Figure 1) display hydrothermal vein intensity changes (spatial frequency of veins) between the hanging wall and footwall, with additional variability along the fault zone itself (Faulkner et al., 2010; Ikari et al., 2009b; Kondo et al., 2005). Assuming veins record fracture and fluid flow, this variability can be interpreted to reflect hydraulic contrasts (e.g., Bons et al., 2022; Ramsay, 1980) and dynamic interplay between deformation and porosity, affecting permeability (e.g., Sibson, 1996). To enable comparison between geological observations and model outputs, we implement a combined tensile fracture and vein formation criterion at each simulation time step. Veins may form at shallow subduction depths through hydrofracturing if fluid volume carries sufficient vein precipitate to fill newly opened cracks (Bons et al., 2022; R. T. Williams & Fagereng, 2022). Such features have been linked to tremor and aseismic slip, suggesting temporal changes in fluid pressure may modulate such events (Akker et al., 2023; Dielforder et al., 2015; Fagereng et al., 2011; Ujiie et al., 2018).

Tensile fracturing is assessed by an overpressure condition (e.g., Otsubo et al., 2020; Secor, 1965):

$$\Delta P = P_f - (\sigma_3 + T_s) \tag{3}$$

and vein formation requires:

$$\Pi = \begin{cases} 1 & \text{if } \Delta P > 0 \quad \wedge \quad \sigma_d < 4T_s \quad \wedge \quad V_\zeta \geq V_{\text{fluid}} \\ 0 & \text{otherwise} \end{cases} \tag{4}$$

Here, $T_s = 10$ MPa is the representative tensile yield strength measured at the current accretionary prism in Nankai Trough (Kitamura et al., 2019), σ_3 is the least principal compressive stress, σ_d is the differential stress ($\sigma_1 - \sigma_3$), and Π is a binary matrix marking potential fracture and vein formation. Although the full principal stress tensor $\boldsymbol{\sigma}$ is resolved, permeability is treated as isotropic and σ_2 does not define a permeability axis. Tensile failure depends solely on σ_3, σ_d, and V_ζ (Equation 4 and Text S3 in Supporting Information S1). Justification of every condition at Equation 4 can be found in Text S3 in Supporting Information S1.

The resulting $\Pi = 1$ field highlights where the hydrofracture criterion has been met such that tensile cracks and veins can potentially occur. The time-integrated normalized intensity of Π defines χ, the cumulative likelihood of vein formation (Text S3 in Supporting Information S1).

3. Results

3.1. Impermeable Models

Field-based observations in some locations, including at the Nobeoka Thrust (Figure 1b), reveal that vein size and intensity tend to increase from the hanging wall to the footwall, and decrease sharply within an impermeable fault core (e.g., Yamaguchi et al., 2011; Figures 1b and 1c). This implies splay faults that act like a barrier to fluid flow (Caine et al., 1996) over multiple seismic cycles. Therefore, our models compute the evolution of stress and pore-fluid pressure P_f over thousands of years, without simulating fault slip or dynamic permeability changes. We define a preferred model with permeability exponents $\gamma_{op} = 8$ (oceanic plate) and $\gamma_{cp} = 5.5$ (continental plate) as they better represent field observations, and we exponentially reduce k toward the SFDZ axis (Figure 3a and Text S2 in Supporting Information S1).

Our results for an impermeable splay fault show that a decrease in vein intensity χ within the SFDZ (Figure 3a) correlates with a transition from dilatant $\left(\dot{\epsilon}_v > 0\right)$ to non-dilatant $\left(\dot{\epsilon}_v \leq 0\right)$ deformation across the hanging wall and footwall (Figure 3c). This transition is accompanied by a drop in overpressure ΔP (Figure 3d) from the footwall into the SFDZ. The footwall is also more dilatant than the hanging wall, and has greater overpressure, consistent with the hydrofracture criterion being more widely achieved in the footwall. Mechanically, enhanced Darcy flux $\vec{q}$ within the footwall (up to $\sim 10^{-9}$–10^{-11} (m/s)) steepens the P_f gradient, sustaining elevated P_f, which reduces effective $(\bar{\sigma})$ and differential (σ_d) stresses while increasing fluid content ζ (Figures 3a–3e). Together, these effects satisfy the hydrofracture and veining conditions of Equation 4.

Within this simplified framework, an impermeable splay fault acts as a hydraulic barrier trapping upwelling fluids from the plate boundary in its footwall. The resulting fluid retention leads to a mechanical transition: the footwall develops a tensile stress regime with $\bar{\sigma}_1 < 0$. In contrast, compressive stresses dominate near the intersection between the splay fault and the megathrust (Figure 3f), where $\bar{\sigma}_1$ reaches up to 25 MPa. In this region, fluid flow is negligible, with velocities on the order of 1×10^{-13} (m/s) (Figure 3e), which decreases P_f (Equation S5 in Supporting Information S1).

If the permeability k of the continental plate increases relative to the preferred model (i.e., decreasing γ_{cp}; Figures 3a–3d), the sealing effect of the fault zone diminishes. The contrast in $\dot{\epsilon}_v$ and ΔP between the hanging wall and footwall is less pronounced, and χ shifts toward a maximum near the hanging wall. Under these conditions, the footwall no longer hosts vein formation, despite having elevated $\dot{\epsilon}_v$ and ΔP. In fact, overpressure levels are nearly an order of magnitude higher than in the preferred model. Such extreme overpressured regimes result in $\sigma_d > 4T_s$ (Figure 3b), thereby violating the hydrofracture condition (Equation 4) and inhibiting vein formation by triggering frictional failure under a static Mohr-Coulomb criterion (Price & Cosgrove, 1990).

Conversely, reducing continental plate permeability (i.e., increasing γ_{cp}; Figures 3a–3d) leads to a decline in fluid supply and therefore restricted ΔP across both the footwall and hanging wall, pushing the system into an underpressured regime ($\Delta P < 0$). Strain rates approach zero, and any positive values of χ are confined to shallow surface layers where the criterion for tensile fracturing is marginally satisfied (Figure S4 in Supporting Information S1). Deeper sections of the model do not attain the necessary overpressure for hydrofracturing, and therefore do not host significant vein development, while small σ_d also makes shear failure unlikely.

3.2. Permeable Models

In the permeable configuration, permeability k increases exponentially toward the SFDZ axis (Figures 3g–3j). This mimics natural cases where the fault zone itself is fractured or foliated and potentially acts as a conduit for fluid flow (Caine et al., 1996). The Inuyama thrust (Figures 1d–1f) may transiently have acted like such a conduit, based on observations of minor veins and hydrothermal precipitates locally within the fault. Similarly, the Pāpaku splay fault drilled offshore along the Hikurangi margin, New Zealand, contains brecciated, likely high permeability layers (Fagereng et al., 2019) although their connectivity may be limited (Clairmont & Fulton, 2025). We adopt the same preferred model used for the impermeable case, employing $\gamma_{op} = 8$ and $\gamma_{cp} = 5.5$. This configuration yields a dilatant and overpressured regime throughout the entire SFDZ. Within these conditions, differential stress exceeds the tensile failure threshold ($\sigma_d > 4T_s$, Figure 3h), enhancing frictional failure under a static Mohr-Coulomb criterion (Price & Cosgrove, 1990) and preventing tensile vein formation in the footwall. In

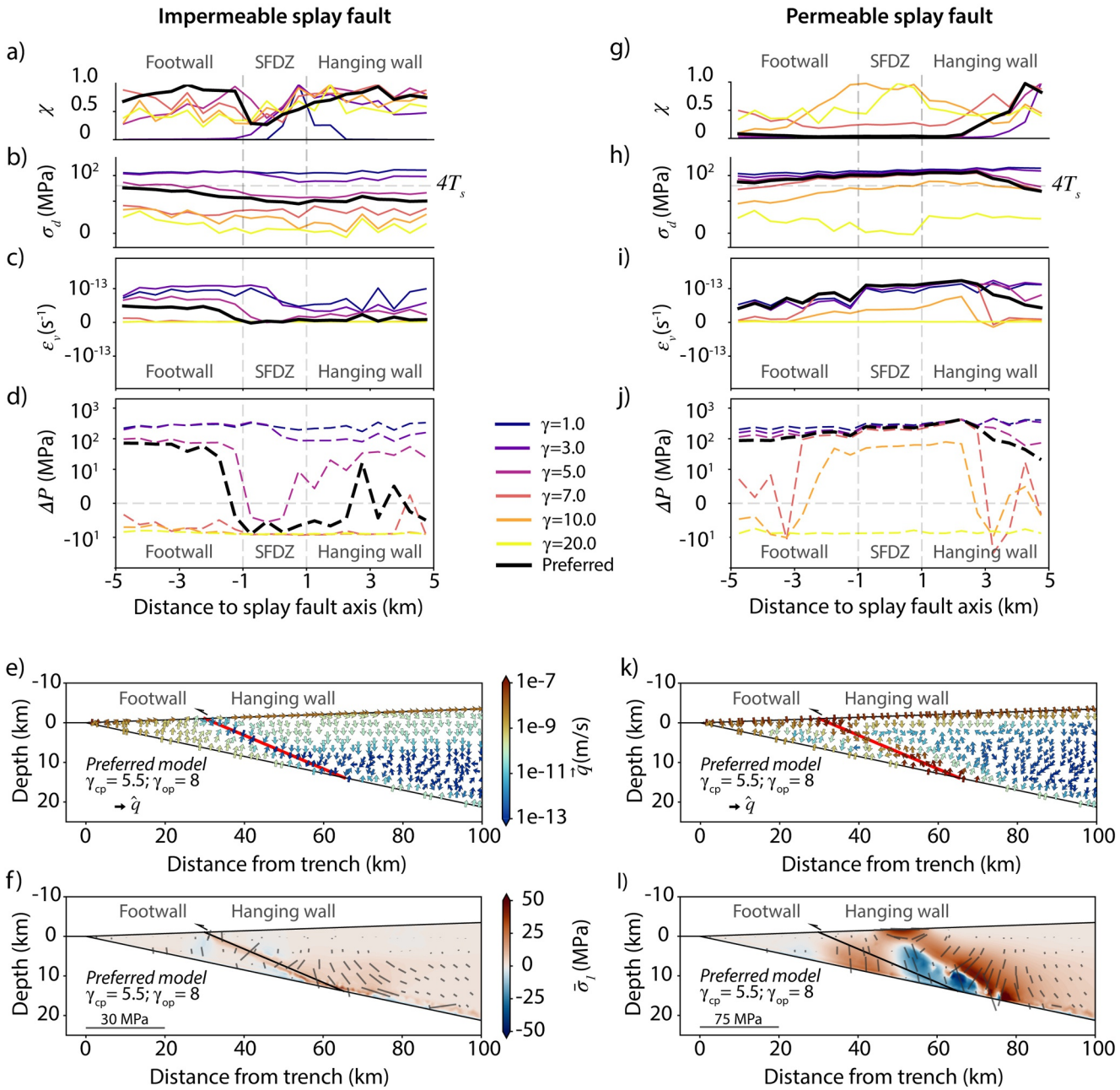

Figure 3. Main results from long-term simulations where each model spans 2,000 years. Panels (a–f) show results with an impermeable splay fault, whereas (g–l) show permeable scenarios. Panels (a, g) are the normalized intensity of veins χ within ±5 (km) of normal distance to the splay fault axis. SFDZ is the *Splay Fault Damage Zone* of $W = 2$ (km). Panels (b–d) and (h–j) show the variability of σ_d, $\dot{\epsilon_v}$, and ΔP. Each colored line represents a model with a different γ_{cp} value, where smaller γ_{cp} leads to a greater bulk permeability (Figure 2c). In (b, h), the horizontal light gray dashed line is the $4T_s$ limit above which tensile fractures will not form. Panels (e, k) show the Darcy's flux $\vec{q}$ for each preferred case. Red lines are the splay fault axis. Arrows are unit vectors $\hat{q}$ colored by their magnitudes. Finally, (f, l) show the long-term regime of the effective greatest compressive principal stress $\bar{\sigma}_1$, for the impermeable and permeable preferred model, respectively. Gray lines represent the orientation and magnitude of $\bar{\sigma}_1$.

contrast, veins emerge within the hanging wall but only at locations more than ∼1 km from the fault core (Figures 3f–3h).

Darcy flux $\vec{q}$ magnitudes reach up to 1×10^{-7} (m/s), particularly at the surface and near the intersection of the splay fault with the plate interface. Opposite to the impermeable fault case, fluid flow in the footwall predominantly trends downward, while upward flow is focused along the SFDZ, exhibiting a channeled pattern

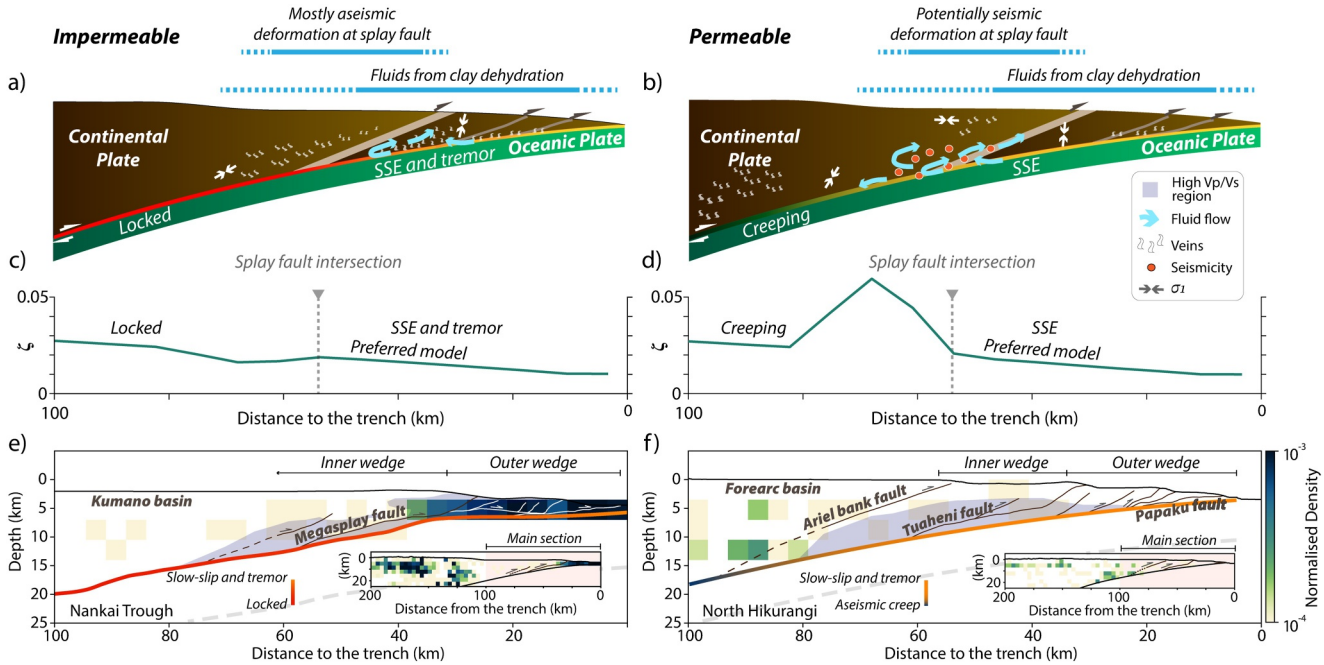

Figure 4. Contrasting behaviors of impermeable and permeable splay faults. Panels (a, b) are schematic models integrating geological and geophysical observations with simulation results. Panels (c, d) show the distribution of fluid content (ζ), extracted along the plate interface using a ±300 (m) normal buffer. Panels (e, f) show trench-perpendicular cross sections at the Nankai Trough (~32°N) and North Hikurangi (~39°S), respectively. Normalized seismicity density is derived from a compilation of earthquake catalogs (Text S4 in Supporting Information S1). Megathrust frictional behavior is based on Takemura et al. (2023) for Nankai and Michel et al. (2025) for North Hikurangi. Slab geometries follow Nakanishi et al. (2018) (Nankai) and C. A. Williams et al. (2013) (Hikurangi). Upper plate structures are compiled from regional seismic profiles (Bangs et al., 2023; Barker et al., 2009; Górszczyk et al., 2025; Plaza-Faverola et al., 2016; Strasser et al., 2009; Tsuji et al., 2014). Solid gray lines are delineated structures and dashed lines are inferred fault traces.

(Figure 3i). This pattern results from the large $\vec{q}$ and consequent increase in the gradient of P_f (Supporting Information S1, Equation S5). The principal stress $\bar{\sigma}_1$ reveals a tensile regime at the splay fault–megathrust intersection, bordered by compressive zones (Figure 3j), with stress magnitudes reaching ±50 MPa in both domains, roughly double the stress magnitudes achieved in the impermeable fault case.

Increasing the continental plate permeability (k_{cp}) reduces contrasts in k between the host rocks and the splay fault, and thus diminishes any channeled flow along the fault. However, this induces only minor variations from the preferred model (Figures 3g–3j). Both the footwall and hanging wall show slight increases in $\dot{\epsilon}_v$, ΔP, and σ_d (Figures 3h–3j), causing the distribution of vein formation intensity χ to migrate away from the SFDZ (Figure 3g).

More significant differences emerge when k_{cp} is reduced. In this case, the SFDZ remains the most permeable zone but with increased permeability contrast with its surroundings, sustaining an overpressured and dilatant regime along the splay fault (Figures 3g–3j). However, an associated decrease in σ_d allows it to fall below the tensile fracture threshold ($\sigma_d < 4T_s$, Figure 3h), thereby enabling vein formation within the SFDZ. As a result, χ approaches 1 along the fault zone. When $\gamma_{cp} = 20$, χ is close to one primarily near the surface (Figure S5 in Supporting Information S1), but it does not represent regions of overpressure, as $\Delta P < 0$ within the footwall.

4. Discussion

We suggest end-member fluid flow and deformation behaviors of splay fault systems in accretionary wedges at subduction zones (Figures 4a and 4b). Impermeable splay fault models show that fluids sourced from the plate interface, likely generated by dewatering and metamorphic dehydration of clays (Saffer & Tobin, 2011, and reference therein), migrate upward as distributed flow of moderate flux (1×10^{-9} to 1×10^{-11} (m/s)), eventually becoming trapped within the splay fault footwall. A direct consequence is the reduction of fluid content ζ at the plate interface (Figure 4c), which enhances plate boundary strength by increasing effective normal stress, thereby promoting megathrust coupling. At the same time, the footwall of the splay fault is dilatant and

overpressured, creating a weak, low effective stress environment along the splay fault. In contrast, permeable models channelize fluid flow along the splay fault, generating differential stresses σ_d exceeding $4T_s$, which favor frictional failure in the upper plate. However, this permeability structure also increases ζ along the plate interface (Figure 4d), potentially reducing effective stress and promoting creep. We evaluate this conceptual framework by comparing these contrasting end-members to ancient and active splay fault systems in accretionary wedges (Figures 1, 4e, and 4f).

4.1. Limitations

Critical processes including fracture-driven pressurization, permeability evolution due to rupture-related damage, and subsequent sealing by mineral precipitation are not captured. These time-dependent changes may strongly influence seismicity patterns and slow slip phenomena, which often reflect transient fault zone evolution (Bangs et al., 2015; Kato et al., 2010; Peng & Gomberg, 2010; Wallace, 2020). Future models could incorporate dynamically evolving permeability to represent cycles of fracturing, fluid redistribution, and vein sealing. Thus, our models are best viewed as simplified time-integrated, end-member scenarios that isolate the effects of permeable versus impermeable splay faults.

We also model only a single splay fault in the outer wedge. While this isolates the effect of permeability, real accretionary wedges include multiple splays with contrasting properties, out-of-sequence thrusts, relays, and heterogeneous sedimentary layering that strongly influence pore pressure architecture (e.g., Gray et al., 2019; Moore et al., 2011). Furthermore, explicit fluid–rock reactions and crack-seal feedbacks are excluded, despite their role in creating and destroying permeability (Sibson, 1996). Supersaturation is assumed via $V_\zeta > V_{\text{fluid}}$, but no constitutive link ties P_f to vein sealing or matrix stiffening. Although we discuss plate boundary fluid flow, this is based on the effect of splay fault permeability and fluid flow along a plate boundary that has a permeability dictated by its host continental and oceanic rocks. Therefore, we again isolate the effect of splay fault permeability, but in a simplified model where any variability in plate boundary permeability is not included.

Taken together, these limitations constrain how confidently we can relate modeled ζ, ΔP, or χ to natural systems. Our interpretations are therefore intended to highlight time-integrated fluid–deformation feedbacks under controlled but simplified conditions, while isolating the potential role of splay fault permeability in governing deformation and brittle failure mode in accretionary wedges.

4.2. Comparison With Geological Observations

The models were inspired by outcrop-scale observations of fluid-related deformation around splay faults. We revisit these observations in light of these results. The Nobeoka Thrust (Figure 1b) displays a marked reduction of vein intensity within its clay-rich fault core (Figure 1c, Otsubo et al., 2016, 2020). This pattern suggests fluid retention beneath a low-permeability barrier and aligns with our preferred impermeable fault model (Figures 3a–3f). A contrasting scenario is observed at the Inuyama thrust, where there are few splay fault-related veins, but pseudotachylyte, cataclasite, and fault zone fractures (Figure 1f) suggest episodically high shear stress and high transient permeability (Ujiie et al., 2021). Although only reflecting the timescale of post-seismic fluid flow, this is reminiscent of the permeable fault case (Figures 3g–3l), and one can argue that the fault structure therefore is dictated predominantly by high permeability episodes.

We interpret the Nobeoka Thrust as representing an impermeable fault-core, while the Inuyama thrust represents a transiently permeable splay fault within a low-permeability host rock ($\gamma \geq 10$ in our models). Combined with our simulations, we identify that at the accretionary prism scale: (a) a persistent low-permeability splay fault fosters overpressuring and vein formation in its footwall, and (b) a persistent or transiently high-permeability splay fault promotes channeled fluid flow and frictional failure in the upper plate. In this context, the Inuyama case underscores that transient permeability changes due to dynamic fracturing may also influence fluid flow and deformation.

4.3. Comparison With Geophysical Data

Lastly, we relate model outcomes to geophysical and geological data from two subduction zones commonly interpreted as low and high permeability end-members: the Nankai Trough, regarded as an impermeable system (e.g., Kinoshita et al., 2014, and references therein), and North Hikurangi, interpreted as a hydraulically relatively

open and porous accretionary prism (e.g., Eberhart-Phillips et al., 2017; Ellis et al., 2015; Gray et al., 2019). Rather than viewing these regions as strict opposites, we frame them as bounding cases that illustrate how splay fault permeability can modulate fluid and stress evolution in accretionary prisms.

4.3.1. Nankai Trough

At Nankai, laboratory and borehole data indicate that the megasplay fault (Figure 4e) is clay-rich and exhibits extremely low permeability ($k < 5 \times 10^{-20}$ $\left(\mathrm{m}^2\right)$) (Ikari et al., 2009a; Tanikawa et al., 2012). Seismic tomography supports elevated V_p/V_s in the megasplay footwall, and tremor and slow-slip events localize along the plate interface (Takemura et al., 2023; Tsuji et al., 2014). These observations suggest a structurally sealed splay fault that promotes overpressuring below it. Our impermeable models reproduce this behavior, and predict that fluids accumulate in the footwall of the splay fault, generating a tensile and dilatant regime that promotes vein formation. These veins may be indicative of tremor-like activity (Akker et al., 2023; Dielforder et al., 2015; Fagereng et al., 2011), a feature that has already been reported and inferred as thrusting at the toe of the wedge (Ma et al., 2024; Tonegawa et al., 2020). Down-dip from the splay fault intersection, the megathrust ζ is reduced by channeling of fluids into the upper plate below the splay (Figure 4c) which lowers the pore-fluid pressure ratio λ, increasing effective stress and promoting locking—a trend consistent with recent interplate coupling models (H. Kimura et al., 2019).

Importantly, our simulations do not generate channelized fluid flow along an impermeable splay fault but rather volumetric flow within its footwall (Figures 3d and 4a). If fault maturity results from repeated slip (Milliner et al., 2025) and progressive mineralogical changes that reduce both permeability and strength (Collettini et al., 2019), the Nankai megasplay likely represents a mature, hydraulically sealed system, characterized by low friction coefficients ($\mu \sim 0.36$–0.44) (Ikari et al., 2009a). This interpretation aligns with core data indicating low hydraulic diffusivity and limited fracture connectivity (Hammerschmidt et al., 2013). Recent stress measurements (Schaible & Saffer, 2025) reveal a near-failure thrust regime within the megasplay, and a normal to strike-slip regime in the décollement at the prism toe. These features are consistent with our impermeable models. Sharp gradients in P_f and deformation regimes across the splay fault likely promote slip transients; however, we caution that additional factors not incorporated in our simulations, such as temperature-dependent rheology and evolving frictional properties, may govern the seismic or aseismic nature of these transients (e.g., Fagereng & Hartog, 2017; Oncken et al., 2021).

4.3.2. North Hikurangi

The northern Hikurangi margin displays elevated V_p/V_s across both hanging wall and footwall of the splay faults (Figure 4f). Recent cores at the Pāpaku fault confirm a relatively permeable megathrust branch (Greve et al., 2021) with a highly fractured hanging wall damage zone (Savage et al., 2021), and a temperature response to borehole outflow that implies local permeability $k > 1.9 \times 10^{-14}$ $\left(\mathrm{m}^2\right)$ (Clairmont & Fulton, 2025). Seismicity is scarce near the trench but intensifies landward of outer wedge faults (Figure 4f). Our permeable models are consistent with this trend: high Darcy fluxes localize at the splay fault, overpressuring the outer wedge and increasing σ_d and the magnitudes of $\bar{\sigma}_1$ (Figures 3i and 3j). Seismicity here may reflect that fluid pressurization drives effective stress reductions, even in the absence of mature sealing structures (Watson et al., 2019).

Geologically, Pāpaku fault cores reveal high porosity ($\phi = 40$–50%) and mixed brittle-ductile deformation, with relatively low clay content (Fagereng et al., 2019). These features suggest a less mature fault architecture than the Nankai megasplay. Traces of seismic slip (Coffey et al., 2021) and elevated k (Clairmont & Fulton, 2025; Watson et al., 2019) further support this interpretation. Our models suggest that such permeability, if connected, allows widespread overpressuring and dilation, enhancing ζ (Figure 4d) and increasing λ across the wedge. If this fluid flow also occurs along the plate interface it leads to reduced plate interface locking, in agreement with recent coupling models (Michel et al., 2025; Wallace, 2020), and consistent with splay faulting above the weakly coupled megathrust (Mountjoy & Barnes, 2011).

5. Conclusions

Our models show that splay fault permeability can play a first-order role in controlling fluid overpressure, deformation, and stress in the outer accretionary wedge. Impermeable, clay-rich, mature splay faults trap fluids in

the footwall, promoting dilation and vein formation below the splay fault. If this flow removes fluids from the plate interface, a consequence is reduced pore pressure and likely coupling of the megathrust downdip of the intersection. In contrast, permeable, less mature faults promote distributed overpressuring, enhance fluid flux through the wedge, and facilitate stress accumulation and relatively high (compared to the impermeable case) differential stresses in the upper plate.

Although splay fault permeability modulates stress, pore-fluid pressure, and the mode of fault slip, mechanical feedbacks between fluid flow, frictional properties, temperature, and fault maturity are factors not captured explicitly in our models and certainly require future efforts. Nonetheless, integrating long-term geological observations, short-term geophysical data, and modeling results suggests that steady-state and transient splay fault permeability provides a diagnostic window into fluid migration and interplate coupling.

Conflict of Interest

The authors declare no conflicts of interest relevant to this study.

Data Availability Statement

PyLith is an open code software and can be found at Aagaard et al. (2025). The codes to generate the mesh, input files, and different scenarios computed in this work can be found at Julve et al. (2025). Geological and geophysical data used in this work can be found at Tisato et al. (2024), Kitajima et al. (2017), Kitajima and Saffer (2014, 2012), Chesley et al. (2023), Konno et al. (2015), S. Kimura et al. (2019), Deep Sea Drilling Project (1989), Gamage and Screaton (2006), Daigle and Dugan (2012), Resilience National Research Institute for Earth Science and Disaster (2019a, 2019b, 2019c), Tonegawa et al. (2020), Yano et al. (2017), Science, GNS (1970), and Japan Meteorological Agency (2023).

Acknowledgments
This work received funding from the project ASPERITY selected by the ERC as a Consolidator Grant, funded by UKRI Frontier Research Grant EP/Y024672/1, and the JSPS KAKENHI Grant 21H05203. We also thank Rachel Lauer and an anonymous reviewer for comments that greatly improved the paper, and the students of Professor Dr. Kohtaro Ujiie from the Graduate School of Science and Technology, University of Tsukuba, for their support on the field campaign that inspired this manuscript. This is Cardiff EARTH CRediT Contribution 55.

References

Aagaard, B., Knepley, M., & Williams, C. (2025). geodynamics/pylith v4.2.0. *Zenodo*. https://doi.org/10.5281/zenodo.14635926

Aagaard, B., Knepley, M. G., & Williams, C. A. (2013). A domain decomposition approach to implementing fault slip in finite-element models of quasi-static and dynamic crustal deformation. *Journal of Geophysical Research: Solid Earth*, *118*(6), 3059–3079. https://doi.org/10.1002/jgrb.50217

Akker, I. V., Schrank, C., Herwegh, M., Berger, A., Jones, M., & Kewish, C. M. (2023). The geometry, spatial distribution and texture of slate-hosted calcite veins in the Helvetic flysch units—insights in structural and fluid processes within a paleo-accretionary complex. *Geochemistry, Geophysics, Geosystems*, *24*(10), e2023GC010873. https://doi.org/10.1029/2023gc010873

Amaefule, J. O., Altunbay, M., Tiab, D., Kersey, D. G., & Keelan, D. K. (1993). Enhanced reservoir description: Using core and log data to identify hydraulic (flow) units and predict permeability in uncored intervals/wells. In *SPE Annual Technical Conference and Exhibition*. https://doi.org/10.2118/26436-ms

Bangs, N. L., McIntosh, K. D., Silver, E. A., Kluesner, J. W., & Ranero, C. R. (2015). Fluid accumulation along the Costa Rica subduction thrust and development of the seismogenic zone. *Journal of Geophysical Research: Solid Earth*, *120*(1), 67–86. https://doi.org/10.1002/2014jb011265

Bangs, N. L., Morgan, J. K., Bell, R. E., Han, S., Arai, R., Kodaira, S., et al. (2023). Slow slip along the Hikurangi margin linked to fluid-rich sediments trailing subducting seamounts. *Nature Geoscience*, *16*(6), 505–512. https://doi.org/10.1038/s41561-023-01186-3

Barbot, S. (2019). Modulation of fault strength during the seismic cycle by grain-size evolution around contact junctions. *Tectonophysics*, *765*, 129–145. https://doi.org/10.1016/j.tecto.2019.05.004

Barker, D. H. N., Sutherland, R., Henrys, S., & Bannister, S. (2009). Geometry of the Hikurangi subduction thrust and upper plate, North Island, New Zealand. *Geochemistry, Geophysics, Geosystems*, *10*(2), Q02007. https://doi.org/10.1029/2008gc002153

Bassett, D., Shillington, D. J., Wallace, L. M., & Elliott, J. L. (2025). Variation in slip behaviour along megathrusts controlled by multiple physical properties. *Nature Geoscience*, *18*, 1–12. https://doi.org/10.1038/s41561-024-01617-9

Bilek, S. L., & Lay, T. (2018). Subduction zone megathrust earthquakes. *Geosphere*, *14*(4), 1468–1500. https://doi.org/10.1130/ges01608.1

Bons, P. D., Cao, D., Riese, T. D., González-Esvertit, E., Koehn, D., Naaman, I., et al. (2022). A review of natural hydrofractures in rocks. *Geological Magazine*, *159*(11–12), 1952–1977. https://doi.org/10.1017/s0016756822001042

Caine, J. S., Evans, J. P., & Forster, C. B. (1996). Fault zone architecture and permeability structure. *Geology*, *24*(11), 1025–1028. https://doi.org/10.1130/0091-7613(1996)024<1025:fzaaps>2.3.co;2

Chesley, C., Naif, S., & Key, K. (2023). Characterizing the porosity structure and gas hydrate distribution at the southern Hikurangi margin, New Zealand from offshore electromagnetic data. *Geophysical Journal International*, *234*(3), 2411–2428. https://doi.org/10.1093/gji/ggad243

Chester, F. M., Chester, J. S., Kronenberg, A. K., & Hajash, A. (2007). Subcritical creep compaction of quartz sand at diagenetic conditions: Effects of water and grain size. *Journal of Geophysical Research*, *112*(B6), B06203. https://doi.org/10.1029/2006jb004317

Chester, J., Lenz, S., Chester, F., & Lang, R. (2004). Mechanisms of compaction of quartz sand at diagenetic conditions. *Earth and Planetary Science Letters*, *220*(3–4), 435–451. https://doi.org/10.1016/s0012-821x(04)00054-8

Civan, F. (2001). Scale effect on porosity and permeability: Kinetics, model, and correlation. *AIChE Journal*, *47*(2), 271–287. https://doi.org/10.1002/aic.690470206

Clairmont, R. D., & Fulton, P. M. (2025). Permeability of the Pāpaku fault within the Hikurangi subduction zone determined from the thermal response to a free flowing well test. *Journal of Geophysical Research: Solid Earth*, *130*(10), e2024JB030965. https://doi.org/10.1029/2024jb030965

Coffey, G. L., Savage, H. M., Polissar, P. J., Meneghini, F., Ikari, M. J., Fagereng, Å., et al. (2021). Evidence of seismic slip on a large splay fault in the Hikurangi subduction zone. *Geochemistry, Geophysics, Geosystems*, *22*(8), e2021GC009638. https://doi.org/10.1029/2021gc009638

Collettini, C., Tesei, T., Scuderi, M., Carpenter, B., & Viti, C. (2019). Beyond Byerlee friction, weak faults and implications for slip behavior. *Earth and Planetary Science Letters*, *519*, 245–263. https://doi.org/10.1016/j.epsl.2019.05.011

Cortés-Rivas, V., Shillington, D. J., Lizarralde, D., & Mark, H. (2025). Interactions between megathrust behavior and forearc deformation in the Andreanof segment of the Aleutian subduction zone, offshore Alaska, USA. *Geology*, *53*(4), 301–305. https://doi.org/10.1130/g52810.1

Daigle, H., & Dugan, B. (2012). Proceedings of the IODP. https://doi.org/10.2204/iodp.proc.333.201.2014

Deep Sea Drilling Project. (1989). Archive of core and site/hole data and photographs from the deep sea drilling project (DSDP). https://doi.org/10.7289/v54m92g2

Dielforder, A., Vollstaedt, H., Vennemann, T., Berger, A., & Herwegh, M. (2015). Linking megathrust earthquakes to brittle deformation in a fossil accretionary complex. *Nature Communications*, *6*(1), 7504. https://doi.org/10.1038/ncomms8504

Eberhart-Phillips, D., Bannister, S., & Reyners, M. (2017). Deciphering the 3-D distribution of fluid along the shallow Hikurangi subduction zone using P-and S-wave attenuation. *Geophysical Journal International*, *211*(2), 1032–1045. https://doi.org/10.1093/gji/ggx348

Ellis, S., Fagereng, Å., Barker, D., Henrys, S., Saffer, D., Wallace, L., et al. (2015). Fluid budgets along the northern Hikurangi subduction margin, New Zealand: The effect of a subducting seamount on fluid pressure. *Geophysical Journal International*, *202*(1), 277–297. https://doi.org/10.1093/gji/ggv127

Fagereng, Å., & Hartog, S. A. M. D. (2017). Subduction megathrust creep governed by pressure solution and frictional–viscous flow. *Nature Geoscience*, *10*(1), 51–57. https://doi.org/10.1038/ngeo2857

Fagereng, Å., Remitti, F., & Sibson, R. H. (2011). Incrementally developed slickenfibers—geological record of repeating low stress-drop seismic events? *Tectonophysics*, *510*(3–4), 381–386. https://doi.org/10.1016/j.tecto.2011.08.015

Fagereng, Å., Savage, H., Morgan, J., Wang, M., Meneghini, F., Barnes, P., et al. (2019). Mixed deformation styles observed on a shallow subduction thrust, Hikurangi margin, New Zealand. *Geology*, *47*(9), 872–876. https://doi.org/10.1130/g46367.1

Faulkner, D., Jackson, C., Lunn, R., Schlische, R., Shipton, Z., Wibberley, C., & Withjack, M. (2010). A review of recent developments concerning the structure, mechanics and fluid flow properties of fault zones. *Journal of Structural Geology*, *32*(11), 1557–1575. https://doi.org/10.1016/j.jsg.2010.06.009

Fisher, Q. J., Casey, M., Clennell, M., & Knipe, R. J. (1999). Mechanical compaction of deeply buried sandstones of the North Sea. *Marine and Petroleum Geology*, *16*(7), 605–618. https://doi.org/10.1016/s0264-8172(99)00044-6

Gamage, K., & Screaton, E. (2006). Characterization of excess pore pressures at the toe of the Nankai accretionary complex, ocean drilling program sites 1173, 1174, and 808: Results of one-dimensional modeling. *Journal of Geophysical Research*, *111*(B4), B04103. https://doi.org/10.1029/2004jb003572

Garagash, D. I. (2021). Fracture mechanics of rate-and-state faults and fluid injection induced slip. *Philosophical Transactions of the Royal Society A*, *379*(2196), 20200129. https://doi.org/10.1098/rsta.2020.0129

Górszczyk, A., Almeida, R., Brossier, R., Métivier, L., & Operto, S. (2025). Constraining the effect of bathymetric high subduction in an accretionary wedge: Evidence from the Tokai area of the Nankai Trough, Japan. *Geochemistry, Geophysics, Geosystems*, *26*(3), e2024GC011754. https://doi.org/10.1029/2024gc011754

Gray, M., Bell, R. E., Morgan, J. V., Henrys, S., Barker, D. H. N., & parties, the IODP Expedition 372 and 375 science. (2019). Imaging the shallow subsurface structure of the North Hikurangi subduction zone, New Zealand, using 2-D full-waveform inversion. *Journal of Geophysical Research: Solid Earth*, *124*(8), 9049–9074. https://doi.org/10.1029/2019jb017793

Greve, A., Kars, M., & Dekkers, M. J. (2021). Fluid accumulation, migration and anaerobic oxidation of methane along a major splay fault at the Hikurangi subduction margin (New Zealand): A magnetic approach. *Journal of Geophysical Research: Solid Earth*, *126*(2), e2020JB020671. https://doi.org/10.1029/2020jb020671

Haeussler, P. J., Armstrong, P. A., Liberty, L. M., Ferguson, K. M., Finn, S. P., Arkle, J. C., & Pratt, T. L. (2015). Focused exhumation along megathrust splay faults in Prince William Sound, Alaska. *Quaternary Science Reviews*, *113*, 8–22. https://doi.org/10.1016/j.quascirev.2014.10.013

Hammerschmidt, S. B., Davis, E. E., Hüpers, A., & Kopf, A. (2013). Limitation of fluid flow at the Nankai trough megasplay fault zone. *Geo-Marine Letters*, *33*(5), 405–418. https://doi.org/10.1007/s00367-013-0337-z

Hasegawa, R., Yamaguchi, A., Fukuchi, R., Hamada, Y., Ogawa, N., Kitamura, Y., et al. (2019). Postseismic fluid discharge chemically recorded in altered pseudotachylyte discovered from an ancient megasplay fault: An example from the Nobeoka Thrust in the Shimanto accretionary complex, SW Japan. *Progress in Earth and Planetary Science*, *6*(1), 36. https://doi.org/10.1186/s40645-019-0281-2

Hommel, J., Coltman, E., & Class, H. (2018). Porosity–permeability relations for evolving pore space: A review with a focus on (bio-) geochemically altered porous media. *Transport in Porous Media*, *124*(2), 589–629. https://doi.org/10.1007/s11242-018-1086-2

Ikari, M. J., Saffer, D. M., & Marone, C. (2009a). Frictional and hydrologic properties of a major splay fault system, Nankai subduction zone. *Geophysical Research Letters*, *36*(20), L20313. https://doi.org/10.1029/2009gl040009

Ikari, M. J., Saffer, D. M., & Marone, C. (2009b). Frictional and hydrologic properties of clay-rich fault gouge. *Journal of Geophysical Research*, *114*(B5), B05409. https://doi.org/10.1029/2008jb006089

Japan Meteorological Agency. (2023). Earthquake monthly report (catalog edition). Retrieved from https://www.data.jma.go.jp/eqev/data/bulletin/index.html

Julve, J., Fagereng, A., Toffol, G., & Ujiie, K. (2025). Splay fault permeability governs fluid–structure interaction in accretionary wedges. *Zenodo*. https://doi.org/10.5281/zenodo.17384876

Kato, A., Iidaka, T., Ikuta, R., Yoshida, Y., Katsumata, K., Iwasaki, T., et al. (2010). Variations of fluid pressure within the subducting oceanic crust and slow earthquakes. *Geophysical Research Letters*, *37*(14), L14310. https://doi.org/10.1029/2010gl043723

Kimura, H., Tadokoro, K., & Ito, T. (2019). Interplate coupling distribution along the Nankai Trough in southwest Japan estimated from the block motion model based on onshore GNSS and seafloor GNSS/a observations. *Journal of Geophysical Research: Solid Earth*, *124*(6), 6140–6164. https://doi.org/10.1029/2018jb016159

Kimura, S., Ito, T., Noda, S., Kaneko, H., Suzuki, K., Yasuda, H., & Minagawa, H. (2019). Water permeability evolution with faulting for unconsolidated turbidite sand in a gas-hydrate reservoir in the Eastern Nankai Trough area of Japan. *Journal of Geophysical Research: Solid Earth*, *124*(12), 13415–13426. https://doi.org/10.1029/2019jb018102

Kinoshita, M., Kimura, G., & Saito, S. (2014). Chapter 4.4.2 seismogenic processes revealed through the Nankai Trough seismogenic zone experiments core, log, geophysics, and observatory measurements. *Developments in Marine Geology*, *7*, 641–670. https://doi.org/10.1016/b978-0-444-62617-2.00021-9

Kirkpatrick, J. D., Fagereng, Å., & Shelly, D. R. (2021). Geological constraints on the mechanisms of slow earthquakes. *Nature Reviews Earth & Environment*, *2*(4), 285–301. https://doi.org/10.1038/s43017-021-00148-w

Kitajima, H., Saffer, D., Sone, H., Tobin, H., & Hirose, T. (2017). In situ stress and pore pressure in the deep interior of the Nankai accretionary prism, integrated ocean drilling program site c0002. *Geophysical Research Letters*, *44*(19), 9644–9652. https://doi.org/10.1002/2017gl075127

Kitajima, H., & Saffer, D. M. (2012). Elevated pore pressure and anomalously low stress in regions of low frequency earthquakes along the Nankai trough subduction megathrust. *Geophysical Research Letters*, *39*(23), L23301. https://doi.org/10.1029/2012gl053793

Kitajima, H., & Saffer, D. M. (2014). Consolidation state of incoming sediments to the Nankai trough subduction zone: Implications for sediment deformation and properties. *Geochemistry, Geophysics, Geosystems*, *15*(7), 2821–2839. https://doi.org/10.1002/2014gc005360

Kitamura, M., Kitajima, H., Sone, H., Hamada, Y., & Hirose, T. (2019). Strength profile of the inner Nankai accretionary prism at IODP site c0002. *Geophysical Research Letters*, *46*(19), 10791–10799. https://doi.org/10.1029/2019gl083732

Kondo, H., Kimura, G., Masago, H., Ohmori-Ikehara, K., Kitamura, Y., Ikesawa, E., et al. (2005). Deformation and fluid flow of a major out-of-sequence thrust located at seismogenic depth in an accretionary complex: Nobeoka thrust in the Shimanto belt, Kyushu, Japan. *Tectonics*, *24*(6), TC6008. https://doi.org/10.1029/2004tc001655

Konno, Y., Yoneda, J., Egawa, K., Ito, T., Jin, Y., Kida, M., et al. (2015). Permeability of sediment cores from methane hydrate deposit in the eastern Nankai trough. *Marine and Petroleum Geology*, *66*, 487–495. https://doi.org/10.1016/j.marpetgeo.2015.02.020

Lauer, R. M., & Saffer, D. M. (2015). The impact of splay faults on fluid flow, solute transport, and pore pressure distribution in subduction zones: A case study offshore the Nicoya Peninsula, Costa Rica. *Geochemistry, Geophysics, Geosystems*, *16*(4), 1089–1104. https://doi.org/10.1002/2014gc005638

Leeman, J. R., Saffer, D. M., Scuderi, M. M., & Marone, C. (2016). Laboratory observations of slow earthquakes and the spectrum of tectonic fault slip modes. *Nature Communications*, *7*(1), 11104. https://doi.org/10.1038/ncomms11104

Ma, Y., Nakata, R., Mochizuki, K., Hashimoto, Y., & Hamada, Y. (2024). Structural control on the shallow tremor distribution linked to seamount subduction: Insights from high-resolution seismic imaging in Hyuga-Nada. *Earth Planets and Space*, *76*(1), 133. https://doi.org/10.1186/s40623-024-02082-9

Michel, S., Jolivet, R., Klein, E., & Maubant, L. (2025). 14 years of slip on the Hikurangi subduction zone. *Journal of Geophysical Research: Solid Earth*, *130*(7), e2024JB030865. https://doi.org/10.1029/2024jb030865

Milliner, C., Avouac, J. P., Dolan, J. F., & Hollingsworth, J. (2025). Localization of inelastic strain with fault maturity and effects on earthquake characteristics. *Nature Geoscience*, *18*, 1–8. https://doi.org/10.1038/s41561-025-01752-x

Moore, G. F., Saffer, D., Studer, M., & Pisani, P. C. (2011). Structural restoration of thrusts at the toe of the Nankai Trough accretionary prism off Shikoku Island, Japan: Implications for dewatering processes. *Geochemistry, Geophysics, Geosystems*, *12*(5), Q0AD12. https://doi.org/10.1029/2010gc003453

Mountjoy, J. J., & Barnes, P. M. (2011). Active upper plate thrust faulting in regions of low plate interface coupling, repeated slow slip events, and coastal uplift: Example from the Hikurangi margin, New Zealand. *Geochemistry, Geophysics, Geosystems*, *12*(1), Q01005. https://doi.org/10.1029/2010gc003326

Muramoto, T., Ito, Y., Miyakawa, A., & Furuichi, N. (2023). Strain and stress accumulation in viscoelastic splay fault and subducting oceanic crust. *Geophysical Research Letters*, *50*(11), e2023GL103496. https://doi.org/10.1029/2023gl103496

Nakanishi, A., Takahashi, N., Yamamoto, Y., Takahashi, T., Citak, S. O., Nakamura, T., et al. (2018). Geology and tectonics of subduction zones: A tribute to Gaku Kimura. *Geological Society of America*, 69–86. https://doi.org/10.1130/2018.2534(04)

NASA Shuttle Radar Topography Mission. (2013). *Shuttle Radar Topography Mission (SRTM) Global*. OpenTopography. https://doi.org/10.5069/G9445JDF

Noda, A. (2016). Forearc basins: Types, geometries, and relationships to subduction zone dynamics. *GSA Bulletin*, *128*(5–6), 879–895. https://doi.org/10.1130/b31345.1

Oncken, O., Angiboust, S., & Dresen, G. (2021). Slow slip in subduction zones: Reconciling deformation fabrics with instrumental observations and laboratory results. *Geosphere*, *18*(1), 104–129. https://doi.org/10.1130/ges02382.1

Otsubo, M., Hardebeck, J. L., Miyakawa, A., Yamaguchi, A., & Kimura, G. (2020). Localized fluid discharge by tensile cracking during the post-seismic period in subduction zones. *Scientific Reports*, *10*(1), 12281. https://doi.org/10.1038/s41598-020-68418-z

Otsubo, M., Miyakawa, A., Kawasaki, R., Sato, K., Yamaguchi, A., & Kimura, G. (2016). Variations in stress and driving pore fluid pressure ratio using vein orientations along megasplay faults: Example from the Nobeoka thrust, Southwest Japan. *Island Arc*, *25*(6), 421–432. https://doi.org/10.1111/iar.12155

Parasnis, D. S. (1960). The compaction of sediments and its bearing on some geophysical problems. *Geophysical Journal of the Royal Astronomical Society*, *3*(1), 1–28. https://doi.org/10.1111/j.1365-246x.1960.tb00062.x

Park, J.-O., Tsuru, T., Kodaira, S., Cummins, P. R., & Kaneda, Y. (2002). Splay fault branching along the Nankai subduction zone. *Science*, *297*(5584), 1157–1160. https://doi.org/10.1126/science.1074111

Peng, Z., & Gomberg, J. (2010). An integrated perspective of the continuum between earthquakes and slow-slip phenomena. *Nature Geoscience*, *3*(9), 599–607. https://doi.org/10.1038/ngeo940

Plaza-Faverola, A., Henrys, S., Pecher, I., Wallace, L., & Klaeschen, D. (2016). Splay fault branching from the Hikurangi subduction shear zone: Implications for slow slip and fluid flow. *Geochemistry, Geophysics, Geosystems*, *17*(12), 5009–5023. https://doi.org/10.1002/2016gc006563

Price, N. J., & Cosgrove, J. W. (1990). *Analysis of geological structures*. Cambridge University Press.

Ramsay, J. G. (1980). The crack–seal mechanism of rock deformation. *Nature*, *284*(5752), 135–139. https://doi.org/10.1038/284135a0

Resilience National Research Institute for Earth Science and Disaster. (2019a). NIED DONET. https://doi.org/10.17598/nied.0008

Resilience National Research Institute for Earth Science and Disaster. (2019b). NIED f-net. https://doi.org/10.17598/nied.0005

Resilience National Research Institute for Earth Science and Disaster. (2019c). NIED hi-net. https://doi.org/10.17598/nied.0003

Saffer, D. M., & Tobin, H. J. (2011). Hydrogeology and mechanics of subduction zone forearcs: Fluid flow and pore pressure. *Annual Review of Earth and Planetary Sciences*, *39*(1), 157–186. https://doi.org/10.1146/annurev-earth-040610-133408

Savage, H. M., & Brodsky, E. E. (2011). Collateral damage: Evolution with displacement of fracture distribution and secondary fault strands in fault damage zones. *Journal of Geophysical Research*, *116*(B3), B03405. https://doi.org/10.1029/2010jb007665

Savage, H. M., Shreedharan, S., Fagereng, Å., Morgan, J. K., Meneghini, F., Wang, M., et al. (2021). Asymmetric brittle deformation at the Pāpaku fault, Hikurangi subduction margin, NZ, IODP expedition 375. *Geochemistry, Geophysics, Geosystems*, *22*(8), e2021GC009662. https://doi.org/10.1029/2021gc009662

Schaible, K. E., & Saffer, D. M. (2025). State of stress across major faults in the Nankai subduction zone estimated from wellbore breakouts. *Journal of Geophysical Research: Solid Earth*, *130*(7), e2024JB030242. https://doi.org/10.1029/2024jb030242

Science, GNS. (1970). New Zealand earthquake catalogue [Dataset]. https://doi.org/10.21420/0s8p-tz38

Secor, D. T. (1965). Role of fluid pressure in jointing. *American Journal of Science*, *263*(8), 633–646. https://doi.org/10.2475/001c.61428

Sibson, R. H. (1996). Structural permeability of fluid-driven fault-fracture meshes. *Journal of Structural Geology*, *18*(8), 1031–1042. https://doi.org/10.1016/0191-8141(96)00032-6

Strasser, M., Moore, G. F., Kimura, G., Kitamura, Y., Kopf, A. J., Lallemant, S., et al. (2009). Origin and evolution of a splay fault in the Nankai accretionary wedge. *Nature Geoscience*, *2*(9), 648–652. https://doi.org/10.1038/ngeo609

Sun, T., Ellis, S., & Saffer, D. (2020). Coupled evolution of deformation, pore fluid pressure, and fluid flow in shallow subduction forearcs. *Journal of Geophysical Research: Solid Earth*, *125*(3), e2019JB019101. https://doi.org/10.1029/2019jb019101

Takemura, S., Hamada, Y., Okuda, H., Okada, Y., Okubo, K., Akuhara, T., et al. (2023). A review of shallow slow earthquakes along the Nankai Trough. *Earth Planets and Space*, *75*(1), 164. https://doi.org/10.1186/s40623-023-01920-6

Tanikawa, W., Mukoyoshi, H., Tadai, O., Hirose, T., Tsutsumi, A., & Lin, W. (2012). Velocity dependence of shear-induced permeability associated with frictional behavior in fault zones of the Nankai subduction zone. *Journal of Geophysical Research*, *117*(B5), B05405. https://doi.org/10.1029/2011jb008956

Terzaghi, K. (1943). Theoretical soil mechanics. https://doi.org/10.1002/9780470172766

Tisato, N., Bland, C. D., Avendonk, H. V., Bangs, N., Garza, H., Alamoudi, O., & Gase, A. (2024). Permeability and elastic properties of rocks from the Northern Hikurangi margin: Implications for slow-slip events. *Geophysical Research Letters*, *51*(2), e2023GL103696. https://doi.org/10.1029/2023gl103696

Tonegawa, T., Yamashita, Y., Takahashi, T., Shinohara, M., Ishihara, Y., Kodaira, S., & Kaneda, Y. (2020). Spatial relationship between shallow very low frequency earthquakes and the subducted Kyushu-Palau ridge in the Hyuga-Nada region of the Nankai subduction zone. *Geophysical Journal International*, *222*(3), 1542–1554. https://doi.org/10.1093/gji/ggaa264

Tsuji, T., Kamei, R., & Pratt, R. G. (2014). Pore pressure distribution of a mega-splay fault system in the Nankai trough subduction zone: Insight into up-dip extent of the seismogenic zone. *Earth and Planetary Science Letters*, *396*, 165–178. https://doi.org/10.1016/j.epsl.2014.04.011

Ujiie, K., Ito, K., Nagate, A., & Tabata, H. (2021). Frictional melting and thermal fracturing recorded in pelagic sedimentary rocks of the Jurassic accretionary complex, central Japan. *Earth and Planetary Science Letters*, *554*, 116638. https://doi.org/10.1016/j.epsl.2020.116638

Ujiie, K., Saishu, H., Fagereng, Å., Nishiyama, N., Otsubo, M., Masuyama, H., & Kagi, H. (2018). An explanation of episodic tremor and slow slip constrained by crack-seal veins and viscous shear in subduction mélange. *Geophysical Research Letters*, *45*(11), 5371–5379. https://doi.org/10.1029/2018gl078374

Walker, R. L., Knepley, M. G., Aagaard, B. T., & Williams, C. A. (2023). Multiphysics modelling in PyLith: Poroelasticity. *Geophysical Journal International*, *235*(3), 2442–2475. https://doi.org/10.1093/gji/ggad370

Wallace, L. M. (2020). Slow slip events in New Zealand. *Annual Review of Earth and Planetary Sciences*, *48*(1), 1–29. https://doi.org/10.1146/annurev-earth-071719-055104

Watson, S. J., Mountjoy, J. J., Barnes, P. M., Crutchley, G. J., Lamarche, G., Higgs, B., et al. (2019). Focused fluid seepage related to variations in accretionary wedge structure, Hikurangi margin, New Zealand. *Geology*, *48*(1), 56–61. https://doi.org/10.1130/g46666.1

Williams, C. A., Eberhart-Phillips, D., Bannister, S., Barker, D. H. N., Henrys, S., Reyners, M., & Sutherland, R. (2013). Revised interface geometry for the Hikurangi subduction zone, New Zealand. *Seismological Research Letters*, *84*(6), 1066–1073. https://doi.org/10.1785/0220130035

Williams, G., & Watts, D. C. (1970). Non-symmetrical dielectric relaxation behaviour arising from a simple empirical decay function. *Transactions of the Faraday Society*, *66*, 80–85. https://doi.org/10.1039/tf9706600080

Williams, R. T., & Fagereng, Å. (2022). The role of quartz cementation in the seismic cycle: A critical review. *Reviews of Geophysics*, *60*(1), e2021RG000768. https://doi.org/10.1029/2021rg000768

Yamaguchi, A., Cox, S. F., Kimura, G., & Okamoto, S. (2011). Dynamic changes in fluid redox state associated with episodic fault rupture along a megasplay fault in a subduction zone. *Earth and Planetary Science Letters*, *302*(3–4), 369–377. https://doi.org/10.1016/j.epsl.2010.12.029

Yano, T. E., Takeda, T., Matsubara, M., & Shiomi, K. (2017). Japan unified hIgh-resolution relocated catalog for earthquakes (JUICE): Crustal seismicity beneath the Japanese islands. *Tectonophysics*, *702*, 19–28. https://doi.org/10.1016/j.tecto.2017.02.017